

SIRAN: Sinkhorn Distance Regularized Adversarial Network for DEM Super-Resolution using Discriminative Spatial Self-Attention

Subhajit Paul Ashutosh Gupta
 Space Applications Centre
 Indian Space Research Organisation

(subhajitpaul, ashutoshg)@sac.isro.gov.in

Abstract

Digital Elevation Model (DEM) is an essential aspect in the remote sensing domain to analyze and explore different applications related to surface elevation information. In this study, we intend to address the generation of high-resolution DEMs using high-resolution multi-spectral (MX) satellite imagery by incorporating adversarial learning. To promptly regulate this process, we utilize the notion of polarized self-attention of discriminator spatial maps as well as introduce a Densely connected Multi-Residual Block (DMRB) module to assist in efficient gradient flow. Further, we present an objective function related to optimizing Sinkhorn distance with traditional GAN to improve the stability of adversarial learning. In this regard, we provide both theoretical and empirical substantiation of better performance in terms of vanishing gradient issues and numerical convergence. We demonstrate both qualitative and quantitative outcomes with available state-of-the-art methods. Based on our experiments on DEM datasets of Shuttle Radar Topographic Mission (SRTM) and Cartosat-1, we show that the proposed model performs preferably against other learning-based state-of-the-art methods. We also generate and visualize several high-resolution DEMs covering terrains with diverse signatures to show the performance of our model.

1. Introduction

The Digital Elevation Model (DEM) is a digital representation of any three-dimensional surface. It is immensely useful in precision satellite data processing, geographic information systems [41], hydrological studies [29], urban planning [34], and many other key applications. The major sources of DEM generation are ter-

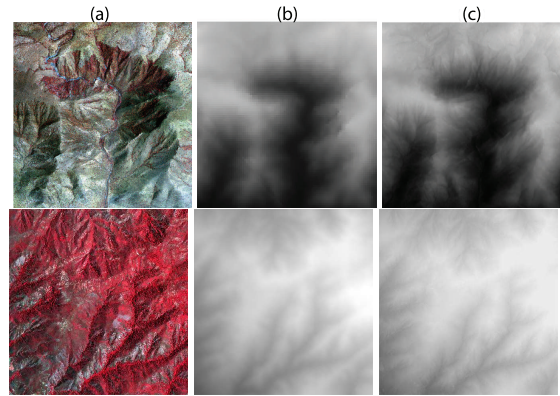


Figure 1. Sample results of DEM super-resolution. (a) High resolution FCC of NIR(R), R(G), and G(B). (b) Bicubic interpolated coarser resolution DEM, (c) Generated High resolution DEM.

restrial, airborne, or space-borne, depending upon the platform used for data acquisition. However, each of these scenarios has its own set of advantages and disadvantages. While elevation models generated using terrestrial and airborne systems have high spatial resolution, their coverage is quite restricted and they typically suffer from several issues and systematic errors [14] [32]. Space-borne missions such as SRTM, and ASTER [1, 13], on the other hand, have almost global coverage but lack the resolution capability at the finest level. Due to the emerging significance and diverse applications of DEM, both its accuracy and resolution have a substantial impact in different fields of operation [27, 39]. However, high-resolution DEM products are expensive, as they require special acquisition and processing techniques to achieve desired results. As an alternative to generating high-resolution DEM from scratch, enhancing the resolution (super-resolution) of existing elevation datasets can be seen as the most optimal strategy to address the shortfall. Hence, we intend to take a step in this di-

rection to generate high-resolution DEM and, to make it more tractable, we formulate this problem in an image super-resolution setting. As shown in Figure 1, our primary objective is to synthesize high-resolution DEM provided its coarser resolution and existing False Colour Composite (FCC) of high-resolution MX imagery.

Recent advances in deep neural networks and optimization techniques show compelling progress over conventionally driven approaches for various computer vision applications like image or video super-resolution. However, we found that very few methods approach the problem of DEM super-resolution, especially, for real-world datasets. We propose a novel framework, which effectively addresses this problem. Our key contributions can be summarized as follows -

1. We propose a novel architecture for DEM super-resolution which effectively utilizes information from a high-resolution MX image as prior by conditioning it with a discriminative spatial self-attention.
2. We develop and demonstrate SIRAN, a framework based on Sinkhorn regularized adversarial learning. We provide theoretical and empirical justification for its effectiveness in resolving the vanishing gradient issue while leveraging tighter iteration complexity.
3. We generate our own dataset by using realistic coarse resolution data instead of bicubic downsampled.
4. Finally, we perform experiments to assess the accuracy of our model along with ablation studies to study the impact of the different configuration choices.

In the following section, we briefly discuss recent works attempting to address similar problem.

2. Related Work

Super-resolution is one of the emerging research fields in the area of computer vision, especially SISR. Interpolation-based techniques like linear, and bicubic are widely used, but they under-perform at high frequency regions producing smoothed outputs [21]. To preserve edge information, multiple reconstruction-based methods like steering kernel regression (SKR) [40] or non-local means (NLM) [35], have also been proposed. Though they can fulfill their primary objective, they cannot produce super-resolved images at a large magnification factor.

DEM is an essential component in remote sensing applications, but research on DEM super-resolution is still limited. Xu *et al.* [45] proposed a super-resolution algorithm based upon NLM. However, after SISR attained the peak of its popularity with the first introduction of Super-resolution using Convolutional Neural Network (SRCNN) [10], its variant D-SRCNN was

proposed by [6] to address the DEM super-resolution problem. It performs better than the non-local-based method. Xu *et al.* [46] brings in the concept of transfer learning where an EDSR (Enhanced Deep Super-Resolution Network) [30], pre-trained over natural images, is taken to obtain a high-resolution gradient map which is fine-tuned to generate high-resolution DEM. After the introduction of Generative Adversarial Network (GAN) by Goodfellow *et al.* [18] a substantial number of methods have evolved in the field of super-resolution like Super-resolution using GANs (SRGAN) [28]. Based on this recently, Benkir *et al.* [8] proposed a DEM super-resolution model, namely D-SRGAN, and later they suggested another model based on EfficientNetV2 [9] for DEM SISR. According to their claim, their proposed methods can outperform the previously mentioned studies in terms of DEM super-resolution.

However, GANs suffer from major issues of mode collapse and vanishing gradients despite providing realistic outcomes. To resolve this, Wasserstein GAN (WGAN) [2] and other variants [20] have been introduced. However, these methods are computationally expensive, which can be untangled by introducing an entropic regularization term [7] resulting in favorable sample complexity [17]. In this study, we explore the efficacy of sinkhorn distance [16] in DEM super-resolution, which is one of the forms of entropic optimal transport.

Guided super-resolution is a prominent research area in computer vision especially in the domain of depth estimation. One of the pioneering works in this domain is [26], where Kim *et al.* proposed Deformable Kernel Networks (DKN) and Faster DKN (FDKN) which learn sparse and spatially invariant filter kernels. Later, He *et al.* [23] exerts a high-frequency guided module to embed the guide details in the depth map. Recently, Metzger *et al.* [33] achieved state-of-the-art performance by adapting the concept of guided anisotropic diffusion with deep convolutional networks. Our proposed method can also be regarded in a similar group where our major attention is to introduce significant features from MX imagery to super-resolved DEM. In the following section, we discuss our overall framework.

3. Methodology

In Figure 2, we have illustrated a detailed architectural overview of our adversarial learning setup. The generator \mathbf{G} operates on upsampled coarser resolution DEM \tilde{x} , MX image prior z , consisting FCC of NIR (R), R (G) and G (B) bands, and PSA of discriminator spatial feature maps, A_s as conditional input. Let $z \sim \mathbb{P}_Z$, where $z \in \mathbb{R}^{H \times W \times 3}$ with \mathbb{P}_Z being the joint distribution of

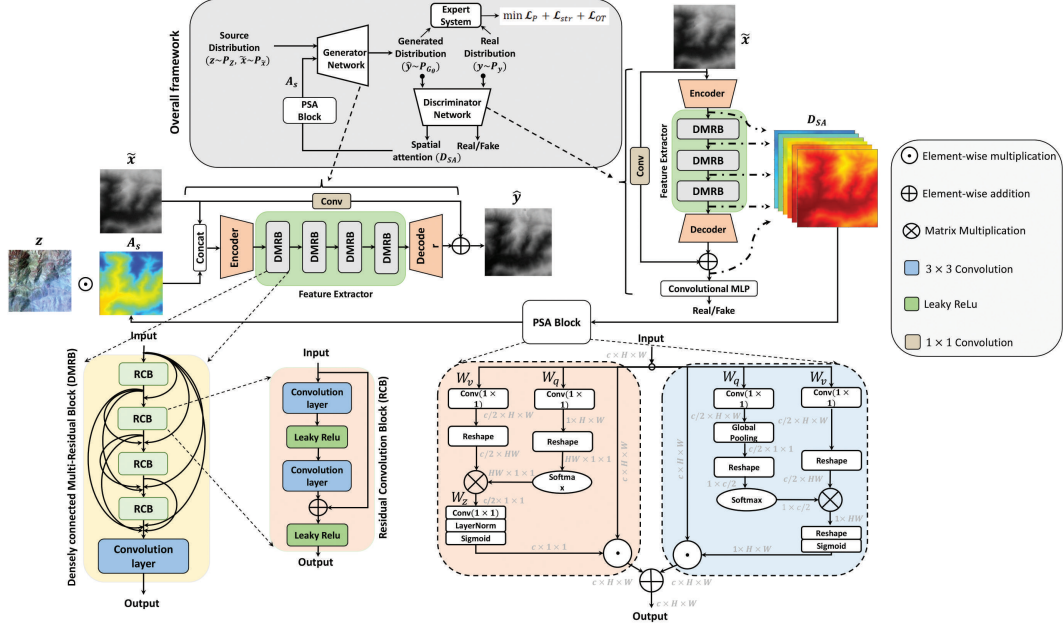


Figure 2. Overview of the proposed adversarial framework with Densely connected Multi Residual Block (DMRB), discriminative spatial attention, Polarized Self-Attention (PSA) block, and loss formulation.

FCC composition and $\tilde{x} \sim \mathbb{P}_{\tilde{x}}$, where $\mathbb{P}_{\tilde{x}}$ constitute of upsampled coarser resolution DEM with $\tilde{x} \in \mathbb{R}^{H \times W}$. Let $\hat{y} \sim \mathbb{P}_{\mathbf{G}_\theta}$, where $\hat{y} = \mathbf{G}(\tilde{x}, z \odot A_s)$, where \odot denotes the element-wise multiplication and $\mathbb{P}_{\mathbf{G}_\theta}$ denotes the generator distribution parameterized by $\theta \in \Theta$. Let $y \sim \mathbb{P}_y$ with \mathbb{P}_y represents the target high resolution DEM distribution. The discriminator \mathbf{D} classifies y and \hat{y} to be coming from real or fake sample space and is assumed to be parameterized by $\psi \in \Psi$.

3.1. Network Architecture

We design both \mathbf{G} and \mathbf{D} models based on ResNet [22] and DenseNet [25]. By combining the idea of skip and dense connections, respectively, we design a building block, namely a Densely connected Multi-Residual Block (DMRB), for our overall framework. Each DMRB block is constituted of multiple densely connected Residual Convolution Block (RCB). DMRB enables efficient context propagation and also stable gradient flow throughout the network. We endorse not using batch normalization as it degrades the performance and gives sub-optimal results for image super-resolution [43] scenarios. We kept the overall design of discriminator \mathbf{D} with a similar configuration as \mathbf{G} with an encoder followed by six DMRBs and finally a decoder to unravel the generated samples properly. The discriminator also adds a Multi-Layer Perceptron (MLP) layer to map its latent features into to required shape. Another reason behind the design of \mathbf{D} is to extract dense discriminative

latent space features, which are passed as conditional input to the generator. In the following subsection, we will briefly explain this module.

3.1.1 Discriminator Spatial Attention

The feature maps from the latent space of the discriminator can be viewed as spatial attention to the generator. Since, the discriminator performs binary classification for a given input, apparently, in latent space, it captures the discriminative features that will help the generator to focus on salient parts of the input images. In [12], the authors introduced this concept of transferring domain-specific latent knowledge of discriminator as spatial attention to the generator. We use this information to condition the prior z to focus on explicit features only.

Therefore, besides classification, \mathbf{D} has another major functional branch, (\mathbf{D}_{SA}), to approximate the spatial attention maps. For any input m , \mathbf{D}_{SA} is used to estimate its corresponding normalized spatial feature maps, $D_{SA} : \mathbb{R}^{H \times W} \rightarrow [0, 1]^{H \times W}$. Let \mathbf{D} consists of k DMRBs and a_i be the activation maps after i^{th} DMRB with c output channels, such that $a_i \in \mathbb{R}^{H \times W \times c}$. Since at different depths, the discriminator focuses on different features, we select k different attention maps from the layers in the latent space. Eventually, attention coefficients are calculated as in [12]:

$$\mathbf{D}_{SA}(m) = \sum_{i=1}^k \sum_{j=1}^c |a_{ij}(m)| \quad (1)$$

We use upsampled coarse resolution DEM \tilde{x} to estimate these attention maps. This choice is motivated by the fact that unlike image-to-image translation in [12], during the test phase, we do not have high-resolution samples in the target domain. For this reason, we use the concept of domain adaptation loss from [38]. These attention maps are passed through a polarized self-attention (PSA) [31] block to exclude redundant features while highlighting significant areas. It is chosen because of its capability to retain the highest internal resolution [31] compared to other self-attention modules. The following section will describe the theoretical framework for optimizing our model.

3.2. Theoretical framework

The overall adversarial framework demonstrated in Figure 2 is trained by optimizing the minmax objective function of a conventional GAN between \mathbf{G} and \mathbf{D} ,

$$\min_{\mathbf{G}} \max_{\mathbf{D}} \mathbb{E}_{y \sim \mathbb{P}_y} [\log(\mathbf{D}(y))] + \mathbb{E}_{\hat{y} \sim \mathbb{P}_{\mathbf{G}_\theta}} [\log(1 - \mathbf{D}(\hat{y}))]. \quad (2)$$

Despite stability issues, we stick with the conventional GAN objective function as in equation 2 due to its ease of implementation and less computational complexity compared to WGANs [2, 20]. In the following subsections, we define the objective function used for training.

3.2.1 Discriminator Objective Function

The objective function of \mathbf{D} in our framework is designed according to equation 2. In addition, we include domain adaptation loss [38] to enforce the discriminator model to mimic the latent features of the high-resolution data and sharpen spatial attention maps provided an upsampled low-resolution data. This loss is defined as

$$\mathcal{L}_{DA} = \mathbb{E}_{\tilde{x} \sim \mathbb{P}_{\tilde{x}}, y \sim \mathbb{P}_y} [\|\mathbf{D}_{SA}(\tilde{x}) - \mathbf{D}_{SA}(y)\|_2^2]. \quad (3)$$

After incorporating domain adaptation loss with adversarial layout, the final objective function of \mathbf{D} becomes

$$\min_{\mathbf{D}} -\mathbb{E}_{y \sim \mathbb{P}_y} [\log(\mathbf{D}(y))] - \mathbb{E}_{\hat{y} \sim \mathbb{P}_{\mathbf{G}_\theta}} [\log(1 - \mathbf{D}(\hat{y}))] + \lambda_{DA} \mathcal{L}_{DA}, \quad (4)$$

where λ_{DA} is the assigned weight for domain adaptation loss in the discriminator loss function.

3.2.2 Generator Objective Function

Apart from the adversarial loss (\mathcal{L}_{ADV}), the objective function of \mathbf{G} is regularized with pixel loss (\mathcal{L}_P) and SSIM loss (\mathcal{L}_{str}) to associate \mathbf{G} to generate samples close to the ground truth. The \mathcal{L}_P ensures minimizing the pixel-wise differences while \mathcal{L}_{str} helps in preserving the perceptual quality and structural information be-

tween the predicted and ground truth images. Although, DEMs have almost no textures, \mathcal{L}_{str} accounts for crucial structural elements like variations in terrain height and slope, and also aids in capturing perceptually significant variations even in minimal texture scenarios to ensure a high-quality representation. These losses are defined below assuming $\hat{y} = \mathbf{G}(\tilde{x}, z \odot A_s(\tilde{x}))$.

$$\begin{aligned} \mathcal{L}_P &= \mathbb{E}_{\tilde{x} \sim \mathbb{P}_{\tilde{x}}, z \sim \mathbb{P}_Z, y \sim \mathbb{P}_y} [\|\hat{y} - y\|_2^2], \\ \mathcal{L}_{str} &= \mathbb{E}_{\tilde{x} \sim \mathbb{P}_{\tilde{x}}, z \sim \mathbb{P}_Z, y \sim \mathbb{P}_y} -\log(\mathbf{SSIM}(\hat{y}, y)), \\ \mathcal{L}_{ADV} &= \mathbb{E}_{\tilde{x} \sim \mathbb{P}_{\tilde{x}}, z \sim \mathbb{P}_Z} -\log(\mathbf{D}(\hat{y})). \end{aligned} \quad (5)$$

The key concern of utilizing an adversarial objective is the vanishing gradient problem near the optimal point. This leads \mathbf{G} to converge to a sub-optimal solution and results in a partially aligned generated distribution with respect to the true distribution. To avoid this, we regularize the generator objective by a distance metric between the generated and target distributions based on the concept of Entropic Optimal Transport (EOT).

Let $\mu_\theta \in \mathbb{P}_{\mathbf{G}_\theta}$ and $\nu \in \mathbb{P}_y$ be the measure of generated and true distribution with support included in a compact bounded set $\mathcal{X}, \mathcal{Y} \subset \mathbb{R}^d$, respectively. Therefore, the EOT [4] between the said measures can be defined using Kantorovich formulation as shown in equation 6 where we assume $\hat{y} = \mathbf{G}_\theta(\tilde{x}, z \odot A_s(\tilde{x}))$.

$$\mathcal{W}_{C, \varepsilon}(\mu_\theta, \nu) = \inf_{\pi \in \Pi(\mu_\theta, \nu)} \mathbb{E}_\pi [C(\hat{y}, y)] + \varepsilon I_\pi(\hat{y}, y),$$

$$\text{where, } I_\pi(\hat{y}, y) = \mathbb{E}_\pi [\log(\frac{\pi(\hat{y}, y)}{\mu_\theta(\hat{y})\nu(y)}), \quad (6)$$

where, $\Pi(\mu_\theta, \nu)$ is the set of all joint distribution on $\mathcal{X} \times \mathcal{Y}$ having marginals μ_θ and ν , $C : \mathcal{X} \times \mathcal{Y} \rightarrow \mathbb{R}$ is the cost of transferring unit mass between locations $\hat{y} \in \mathcal{X}$ and $y \in \mathcal{Y}$, and the regularization term $I_\pi(\cdot)$ is the mutual information between two distribution measures (μ_θ, ν) [15] with ε being its weight factor. When the cost $C(\cdot)$ is chosen as a distance-metric the solution of equation 6 is referred to as entropic Wasserstein distance between two probability measures. The main reason behind considering EOT is due to its favorable sample complexity of $\mathcal{O}(n^{-1/2})$ [17], given a sample size n , compared to $\mathcal{O}(n^{-2/d})$ [44] for OT which is the baseline principle of [2, 20].

To fit the generated measure μ_θ to the true measure ν , we have to minimize the entropic Wasserstein distance between them and this can be treated as an objective function for the generator [3]. However, it has one major issue of being strictly larger than zero even if μ_θ and ν are exactly aligned, i.e. $\mathcal{W}_{C, \varepsilon}(\nu, \nu) \neq 0$. This is resolved by adding normalizing terms to equation 6,

which leads to the Sinkhorn loss [16] as defined below.

$$\mathcal{S}_{C,\varepsilon} = \mathcal{W}_{C,\varepsilon}(\mu_\theta, \nu) - \frac{1}{2}\mathcal{W}_{C,\varepsilon}(\mu_\theta, \mu_\theta) - \frac{1}{2}\mathcal{W}_{C,\varepsilon}(\nu, \nu), \quad (7)$$

Based on the value of ε , equation 7 shows asymptotic behaviour [16]. When $\varepsilon \rightarrow 0$, it recovers the conventional OT problem, while $\varepsilon \rightarrow \infty$, it converges to maximum mean discrepancy (MMD) [19]. Therefore, the Sinkhorn loss interpolates between OT loss and MMD loss as ε varies from 0 to ∞ . Therefore, by properly tuning ε we can leverage the concurrent advantage of non-flat geometric properties of OT loss and, high dimensional rigidity and energy distance properties of MMD loss (when $C = \|\cdot\|_p$ with $1 < p < 2$) by only utilizing Sinkhorn loss. Apart from this, the selection of ε also affects the overall gradients of \mathbf{G} , which eventually results in preventing vanishing gradient problems near the optimal point. This claim can be established from the smoothness property of $\mathcal{S}_{C,\varepsilon}(\mu_\theta, \nu)$ with respect to θ . In this context, we propose **Theorem 1**, where we derive a formulation to estimate the smoothness of Sinkhorn loss.

Theorem 1 (Smoothness of Sinkhorn loss). *Consider the Sinkhorn loss $\mathcal{S}_{C,\varepsilon}(\mu_\theta, \nu)$ between two measures μ_θ and ν on \mathcal{X} and \mathcal{Y} two bounded subsets of \mathbb{R}^d , with a C^∞ , L_0 -Lipschitz, and L_1 -smooth cost function C . Then, for $(\theta_1, \theta_2) \in \Theta$, one has,*

$$\begin{aligned} & \mathbb{E} \|\nabla_\theta \mathcal{S}_{C,\varepsilon}(\mu_{\theta_1}, \nu) - \nabla_\theta \mathcal{S}_{C,\varepsilon}(\mu_{\theta_2}, \nu)\| \\ &= \mathcal{O}\left(L\left(L_1 + \frac{2L_0^2 L}{\varepsilon(1 + Be^{\frac{L}{\varepsilon}})}\right)\|\theta_1 - \theta_2\|\right), \end{aligned} \quad (8)$$

where L is the Lipschitz in θ corresponding to \mathbf{G} , $\kappa = 2(L_0|\mathcal{X}| + \|C\|_\infty)$, $B = d \cdot \max(\|m\|, \|M\|)$ with m and M being the minimum and maximum values in set \mathcal{X} . Let Γ_ε represent the smoothness mentioned above, then we get the following asymptotic behavior in ε :

1. as $\varepsilon \rightarrow 0$, $\Gamma_\varepsilon \rightarrow \mathcal{O}\left(\frac{2L_0^2 L^2}{Be^{\frac{L}{\varepsilon}}}\right)$
2. as $\varepsilon \rightarrow \infty$, $\Gamma_\varepsilon \rightarrow \mathcal{O}(LL_1)$

Proof. Refer to Appendix A. \square

Theorem 1 shows the variation of smoothness of $\mathcal{S}_{C,\varepsilon}(\mu_\theta, \nu)$ with respect to ε . Using this, we can estimate the upper bound of the overall expected gradient of our proposed adversarial set-up. Hence, to formulate this upper bound, we present **Proposition 1**.

Proposition 1. *Let $l(\cdot)$, $g(\cdot)$ and $\mathcal{S}_{C,\varepsilon}(\cdot)$ be the objective functions related to supervised losses, adversarial loss and Sinkhorn loss respectively, and θ^* and ψ^* be the parameters of optimal generator \mathbf{G} and discriminator \mathbf{D} . Let us suppose $l(p, y)$, where $p = \mathbf{G}_\theta(x)$, is β -smooth in p . If $\|\theta - \theta^*\| \leq \epsilon$ and*

$\|\psi - \psi^\| \leq \delta$, then $\|\nabla_\theta \mathbb{E}_{(x,y) \sim \mathcal{X} \times \mathcal{Y}} [l(\mathbf{G}_\theta(x), y) + \mathcal{S}_{C,\varepsilon}(\mu_\theta(\mathbf{G}_\theta(x)), \nu(y)) - g(\psi; \mathbf{G}_\theta(x))]\| \leq L^2\epsilon(\beta + \Gamma_\varepsilon) + L\delta$, where Γ_ε is the derived smoothness of Sinkhorn loss in equation 8.*

Proof. Refer to Appendix B. \square

In a traditional adversarial set-up as mentioned in [37], $\epsilon \rightarrow 0$ suggests reductions of δ , which eventually results in a vanishing gradient near the optimal region. However, in our Sinkhorn regularized adversarial framework, the upper bound is also dependent on Γ_ε as exhibited in **Proposition 1**. From equation 8, Γ_ε is exponentially variable with respect to the choice of ε . Hence, the selection of adequate ε will have a profound impact in mitigating the vanishing gradient problem suffered by regular adversarial setup.

Apart from resolving the vanishing gradient problem, our Sinkhorn regularized adversarial set-up leads to faster numerical convergence of the supervised loss resulting in more stringent iteration complexity [37]. Therefore, we present **Proposition 2** to deduce the iteration complexity of our proposed adversarial framework.

Proposition 2. *Suppose the supervised loss $l(\theta)$ is lower bounded by $l^* > -\infty$ and it is twice differentiable. For some arbitrarily small $\zeta > 0$, $\eta > 0$ and ϵ_1 -stationary point with $\epsilon_1 > 0$, let $\|\nabla g(\psi; \mathbf{G}_\theta(x))\| \geq \zeta$, $\|\nabla \mathcal{S}_{C,\varepsilon}(\mu_\theta(\mathbf{G}_\theta(x)), \nu(y))\| \geq \eta$ and $\|\nabla l(\mathbf{G}_\theta(x), y)\| \geq \epsilon_1$, with conditions $\delta \leq \frac{\sqrt{2\epsilon_1\zeta}}{L}$, and $\Gamma_\varepsilon < \frac{\sqrt{2\epsilon_1\eta}}{L^2\epsilon}$, then the iteration complexity in Sinkhorn regularized adversarial framework is upper bounded by $\mathcal{O}\left(\frac{(l(\theta_0) - l^*)\beta_1}{\epsilon_1^2 + 2\epsilon_1(\zeta + \eta) - L^2(\delta^2 + L^2\Gamma_\varepsilon^2\epsilon^2)}\right)$, assuming $\|\nabla^2 l(\theta)\| \leq \beta_1$.*

Proof. Refer to Appendix C. \square

Corollary 1. *Using first order Taylor series, the upper bound in **Proposition 2** becomes $\mathcal{O}\left(\frac{l(\theta_0) - l^*}{\epsilon_1^2 + \epsilon_1(\zeta + \eta)}\right)$.*

Proof. Refer to Appendix C.1. \square

Since the denominator of the derived upper bound in **Proposition 2** is greater than the one mentioned in Theorem 3 of [37], we can infer that our proposed learning framework has tighter iteration complexity compared to the general adversarial setup. This is only true when $\Gamma_\varepsilon < \frac{\sqrt{2\epsilon_1\eta}}{L^2\epsilon}$, and it can be easily satisfied by appropriate choice of ε . It can also be verified using a simpler setup as shown in **Corollary 1**, as it increases the convergence rate from $\mathcal{O}((\epsilon_1^2 + \epsilon_1\zeta)^{-1})$ [37] to $\mathcal{O}((\epsilon_1^2 + \epsilon_1(\zeta + \eta))^{-1})$ which effects considerably in the training iterations as shown in section 5.3 as well as in appendix D. This also

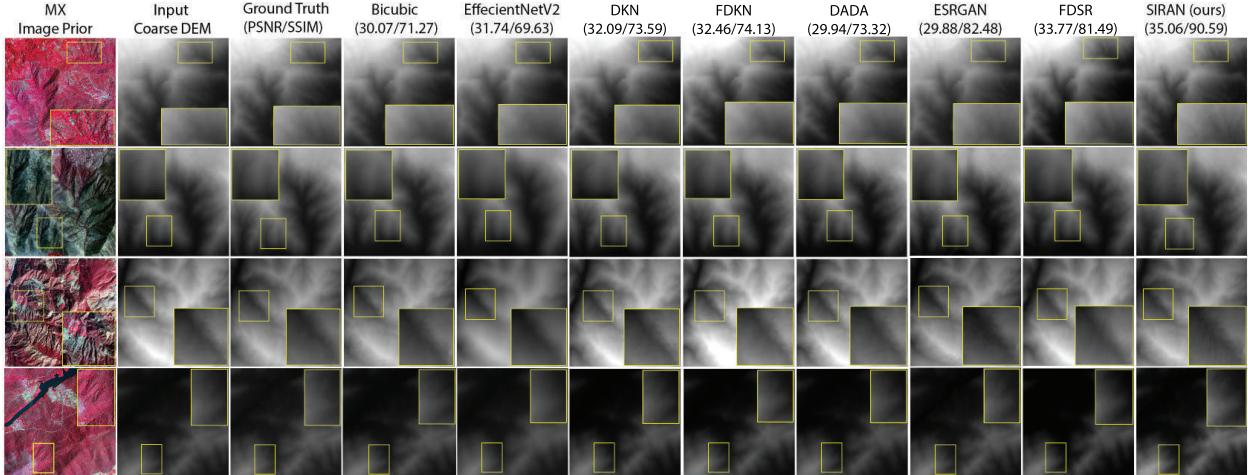


Figure 3. Results (inside India) for DEM super-resolution (better viewed at 200%) and comparisons with other baseline methods.

suggests that our setup is equivalent to applying two discriminator operations without involving additional computations which helps in effectively leveraging the advantage of using multiple discriminators [11]. Due to lack of space, experiment results to support the proposed theorem and propositions are carried out in Appendix D.

Due to the mentioned advantages, we have regularized the overall generator loss with Sinkhorn distance which is defined below assuming $\hat{y} = \mathbf{G}(\tilde{x}, z \odot A_s(\tilde{x}))$.

$$\mathcal{L}_{OT} = \mathbb{E}_{\tilde{x} \sim \mathbb{P}_{\tilde{x}}, z \sim \mathbb{P}_z, y \sim \mathbb{P}_y} \mathcal{S}_{C, \varepsilon}(\mu(\hat{y}), \nu(y)), \quad (9)$$

where μ and ν represent the measure of generated and true distributions, respectively. \mathcal{L}_{OT} is estimated according to [16] which utilizes ε and the Sinkhorn iterations T as the major parameters. Therefore, the overall generator loss can be defined as,

$$\lambda_P \mathcal{L}_P + \lambda_{str} \mathcal{L}_{str} + \lambda_{ADV} \mathcal{L}_{ADV} + \lambda_{OT} \mathcal{L}_{OT}, \quad (10)$$

where λ_P , λ_{str} , λ_{ADV} and λ_{OT} represent the weight assigned to pixel loss, SSIM loss, adversarial loss, and Sinkhorn loss respectively.

4. Experiments

In this section, we discuss experiments to analyze the efficacy of our proposed model in DEM super-resolution.

4.1. Datasets

DEM super-resolution is a relatively unexplored area that suffers from a lack of realistic datasets. Therefore, in this study, we generate our own DEM super-resolution dataset. From the real-world application point of view, we leverage to use real coarse resolution SRTM DEM with a ground sampling distance (GSD) of 30m

as input instead of conventional bicubic downsampled while taking Indian high-resolution DEM (GSD=10m) generated from Cartosat-1 stereoscopic satellite, as the ground truth. For the image prior, we utilize the high-resolution MX data (GSD=1.6m) from the Cartosat-2S satellite. The DEMs are upsampled to the resolution of MX images using bicubic interpolation to generate a paired dataset. This helps in increasing the training samples as well as assists the model to learn dense high-resolution features from the prior. The dataset consists of 72,000 patches of size (256, 256), which includes various signatures such as vegetation, mountains, and, water regions. We use 40,000 samples for training, 20,000 for cross-validation, and 12,000 for testing, where 10,000 patches belong to the Indian subcontinent region and the rest outside India. As ground truth DEM data is only available for Indian regions, our model is trained on limited landscape areas. To check its generalization capability, we also test our model on data from outside India from the Fallbrook region, US, where Cartosat DEM data is unavailable. For these cases, we validate our result based on available 10m DEM data of the 3D Elevation Program (3DEP) [42].

4.2. Implementation Details

All the experiments are conducted under identical environments. We use 3×3 convolution kernel and leaky ReLU activation except in global skip connection where 1×1 kernel is used without any activation. Each DMRB has 64 convolution operations. We use ADAM optimizer with a fixed learning rate of 0.0001. During adversarial training, we update the critic once every single update in the generator. We set $\lambda_{DA} = 0.1$, $\lambda_P = 100$, $\lambda_{str} = 1$, $\lambda_{ADV} = 1$ and $\lambda_{OT} = 0.01$. For estimating

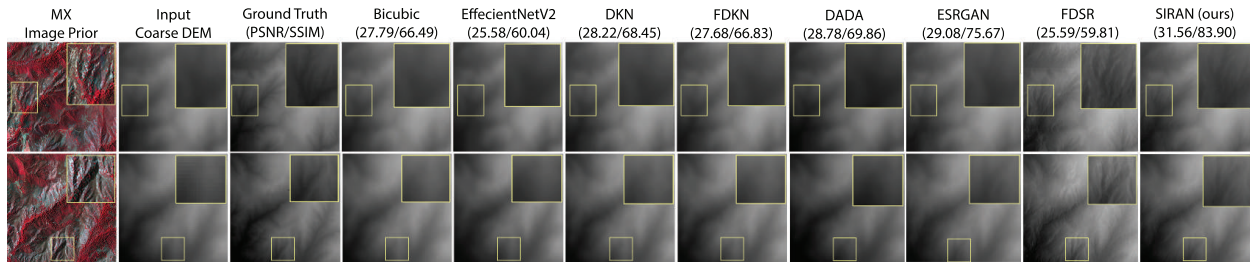


Figure 4. Results (outside India) for DEM super-resolution (better viewed at 200%) and comparisons with other baseline methods.

\mathcal{L}_{OT} , we set $T = 10$ and $\varepsilon = 0.1$. The entire framework is developed using PyTorch. All the experiments are performed on 2 Nvidia V100 GPUs. During testing, our model takes 0.46s for a single patch in one GPU.

5. Result Analysis

In this section, we analyze both qualitatively and quantitatively, the quality of our proposed super-resolved DEMs. We compare it with traditional bicubic as well as other learning-based state-of-the-art methods [8, 9] which also includes recent baseline models for image-guided depth super-resolution [23, 26, 33].

Table 1. Quantitative comparison with state-of-the-art methods for both patches of inside and outside India. First and second methods are highlighted in red and green, respectively.

| Method | RMSE (m) | | MAE (m) | | SSIM(%) | | PSNR | |
|--------------|----------|---------|---------|---------|---------|---------|--------|---------|
| | Inside | Outside | Inside | Outside | Inside | Outside | Inside | Outside |
| Bicubic | 15.25 | 23.19 | 12.42 | 22.04 | 71.27 | 66.49 | 30.07 | 27.79 |
| ENetV2 [9] | 20.35 | 30.53 | 18.72 | 28.36 | 69.63 | 60.04 | 31.74 | 25.58 |
| DKN [26] | 12.89 | 21.16 | 11.18 | 19.78 | 73.59 | 68.45 | 32.09 | 28.22 |
| FDKN [26] | 13.05 | 21.93 | 11.34 | 20.41 | 74.13 | 66.83 | 32.46 | 27.68 |
| DADA [33] | 37.49 | 40.89 | 32.17 | 37.74 | 73.32 | 69.86 | 27.94 | 26.78 |
| ESRGAN [8] | 31.33 | 20.45 | 25.56 | 18.34 | 82.48 | 75.67 | 29.88 | 29.05 |
| FDSR [23] | 12.98 | 30.58 | 10.87 | 25.28 | 81.49 | 59.81 | 33.77 | 25.59 |
| SIRAN (ours) | 9.28 | 15.74 | 8.51 | 12.25 | 90.59 | 83.90 | 35.06 | 31.56 |

5.1. Quantitative Analysis

To quantitatively analyze the outcomes of DEM super-resolution, we use RMSE, MAE, PSNR, and SSIM as evaluation metrics. Our proposed method outperforms other state-of-the-art methods, as illustrated in Table 1. For both inside and outside India patches, our method not only retains the elevation values but also captures high-resolution structural details with fidelity. This results in more than 24% improvement in RMSE and MAE, 8% in SSIM, and 4% in PSNR with respect to the second best in each criterion. Despite having different source domains for reference DEM for patches outside India, our method performs substantially in generating high-resolution DEM as depicted in the above table which suggests better generalization capability of our model compared to others. Among the other methods, FDSR [23] performs closely to our model for Indian patches. However, for outside patches, its perfor-

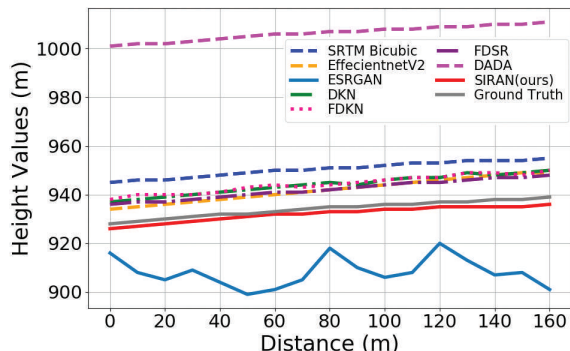


Figure 5. Line profile analysis of SIRAN and other baselines.

mance deteriorates. Although ESRGAN captures the high structural details, it has poor RMSE and MAE due to the presence of noise. In Figure 5, we have demonstrated the line profile analysis of SIRAN as well as other baseline models with respect to the ground truth. Compared to others, SIRAN not only has the lowest bias but also follows the true elevation values most closely. This supports the error analysis in Table 1.

5.2. Qualitative Analysis

Figure 3 demonstrates the qualitative analysis of our proposed method for patches of India. Compared to other approaches, SIRAN is able to highlight key features and retain the perceptual quality with respect to ground truth. ESRGAN also captures substantial structural information in its outcomes, however, it tends to produce artifacts and noise in the generated DEM which is depicted in Table 1 and Figure 5. In Figure 4, we have compared the outcomes for patches from outside India. As indicated before, compared to other baseline techniques, our method is able to generate higher resolution DEM in close proximity to the reference DEM despite having a different source domain. Although FDSR [23] performed well for Indian patches, due to lack of generalization capability it introduces image details more prominently in the generated DEM for test patches outside India. In Figure 6, we demonstrate 3-D visualization of generated DEMs, corresponding to

Table 2. Quantitative analysis for the effect of introducing different modules for DEM super-resolution

| Image Prior | Spatial Attention | PSA | Sinkhorn loss | RMSE (m) | MAE (m) | SSIM (%) | PSNR |
|-------------|-------------------|-----|---------------|-------------|-------------|--------------|--------------|
| X | X | X | X | 16.54 | 13.63 | 72.27 | 30.25 |
| ✓ | X | X | X | 29.32 | 25.41 | 78.29 | 28.25 |
| ✓ | ✓ | X | X | 20.76 | 18.29 | 81.68 | 31.08 |
| ✓ | ✓ | ✓ | X | 18.76 | 15.13 | 85.04 | 32.21 |
| ✓ | ✓ | ✓ | ✓ | 9.28 | 8.51 | 90.49 | 35.06 |

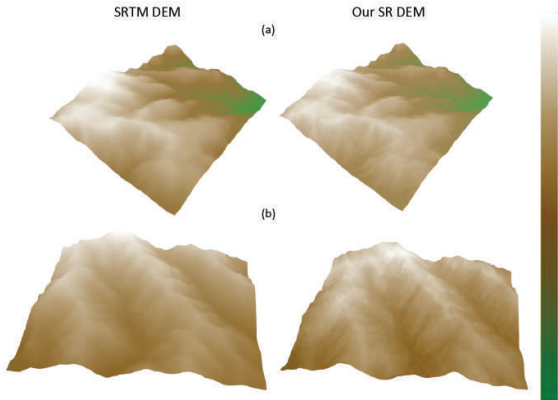


Figure 6. Illustration of 3-D visualization of Super-resolved and SRTM DEM

a region, where ground truth is unavailable. We compare it with available SRTM DEM, and clearly, our topographic view of generated DEM captures sharper features in mountainous regions as well as in the tributaries of the water basin area as shown in Figure 6.

5.3. Ablation Study

In this section, we analyze the efficacy of our four proposed modules, image prior, spatial attention from discriminator, PSA, and Sinkhorn loss-based adversarial learning. In the absence of any prior, it leads to outcomes similar to bicubic interpolation that affects its SSIM score as shown in Table 2. Using high-resolution MX image priors resolves this issue to a certain extent by increasing SSIM by more than 6%. Yet, this degrades the performance of the model in terms of RMSE and MAE. To improve upon this situation, we introduce spatial feature maps from the discriminator. Figure 7 shows how individual attention maps after each DMRB prioritizes certain features at different labels. However, the mean attention weights are approximately uniform as shown in Figure 8. PSA handles this matter by emphasizing key features. Addressing both these attentions improves the RMSE and MAE by more than 50% as well as enhances SSIM by almost 7% as shown in Table 2. The introduction of Sinkhorn distance regularization enhances the evaluation parameters further with both MAE

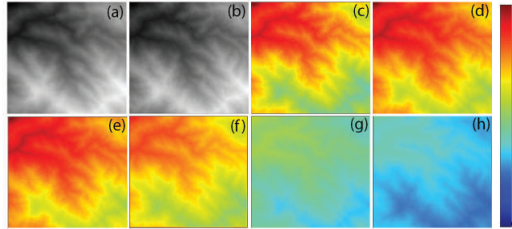


Figure 7. (a) Source, (b) Target, (c)-(h) Discriminator spatial attention after each DMRB from top to bottom.

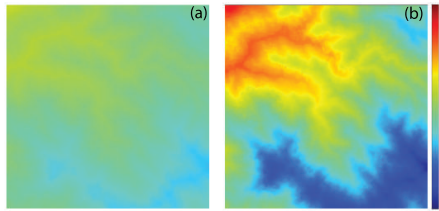


Figure 8. (a) Weights of mean discriminator spatial attention (D_{SA}), (b) weights after passing D_{SA} through PSA block

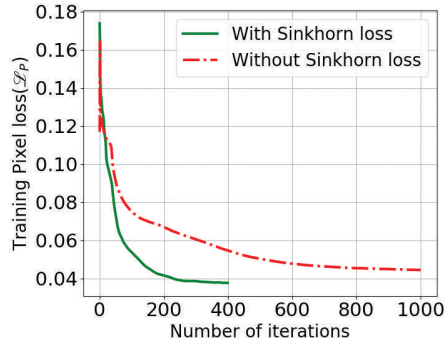


Figure 9. Effect of sinkhorn loss in training convergence

and RMSE below 10 m and SSIM more than 90% as shown in Table 2. Apart from this, sinkhorn loss also contributed to a near 2.5X faster convergence rate for the pixel loss as shown in Figure 9. This also supports our argument in **Proposition 2**.

6. Conclusions

In this paper, we demonstrated an effective approach for DEM super-resolution using realistic coarse data samples. Unlike regular SISR, the method uses high-resolution MX images as prior in a specially designed architectural framework consisting of spatial attention maps from discriminator, PSA, and DMRBs, optimized using Sinkhorn distance regularized adversarial learning. We provided theoretical and empirical evidence to show how this choice stabilizes the training of our adversarial model and improves its convergence. We perform quantitative and qualitative analysis by generating and comparing DEMs related to different signatures along with investigating generalization

capability by testing out-of-domain samples. We also analyse how each proposed module affects the outcomes. Our method achieves favorable results compared to other state-of-the-art methods. In the future, we would like to investigate the effect of Sinkhorn loss on sub-optimality gap and generalization error.

References

- [1] Michael Abrams, Robert Crippen, and Hiroyuki Fujisada. Aster global digital elevation model (gdem) and aster global water body dataset (astwbd). *Remote Sensing*, 12(7), 2020. [1](#)
- [2] Martin Arjovsky, Soumith Chintala, and Léon Bottou. Wasserstein generative adversarial networks. In *Proceedings of the 34th International Conference on Machine Learning*, pages 214–223. PMLR, 2017. [2](#), [4](#)
- [3] Martin Arjovsky, Soumith Chintala, and Léon Bottou. Wasserstein gan, 2017. [4](#), [5](#)
- [4] Genevay Aude, Marco Cuturi, Gabriel Peyré, and Francis Bach. Stochastic optimization for large-scale optimal transport, 2016. [4](#)
- [5] Genevay Aude, Marco Cuturi, Gabriel Peyré, and Francis Bach. Stochastic optimization for large-scale optimal transport, 2016. [1](#)
- [6] Zixuan Chen, Xuewen Wang, Zekai Xu, and Hou Wenguang. Convolutional neural network based dem super resolution. *ISPRS - International Archives of the Photogrammetry, Remote Sensing and Spatial Information Sciences*, XLI-B3:247–250, 2016. [2](#)
- [7] Marco Cuturi. Sinkhorn distances: Lightspeed computation of optimal transportation distances. *Advances in Neural Information Processing Systems*, 26, 2013. [2](#), [1](#)
- [8] Bekir Z. Demiray, Muhammed Ali Sit, and Ibrahim Demir. D-SRGAN: DEM super-resolution with generative adversarial networks. *CoRR*, abs/2004.04788, 2020. [2](#), [7](#)
- [9] Bekir Z Demiray, Muhammed Sit, and Ibrahim Demir. Dem super-resolution with efficientnetv2, 2021. [2](#), [7](#)
- [10] Chao Dong, Chen Change Loy, Kaiming He, and Xiaoou Tang. Image super-resolution using deep convolutional networks. *IEEE Transactions on Pattern Analysis and Machine Intelligence*, 38, 2014. [2](#)
- [11] Ishan P. Durugkar, Ian Gemp, and Sridhar Mahadevan. Generative multi-adversarial networks. *CoRR*, abs/1611.01673, 2016. [6](#)
- [12] Hajar Emami, Majid Moradi Aliabadi, Ming Dong, and Ratna Babu Chinnam. SPA-GAN: spatial attention GAN for image-to-image translation. *CoRR*, abs/1908.06616, 2019. [3](#), [4](#)
- [13] T. G. Farr and M. Kobrick. Shuttle radar topography mission produces a wealth of data. *Eos Trans. AGU*, 81:583–583, 2000. [1](#)
- [14] Peter Fisher and Nicholas Tate. Causes and consequences of error in digital elevation models. progress in physical geography. *Progress in Physical Geography*, 30, 2006. [1](#)
- [15] Aude Genevay, Marco Cuturi, Gabriel Peyré, and Francis R. Bach. Stochastic optimization for large-scale optimal transport. *ArXiv*, abs/1605.08527, 2016. [4](#)
- [16] Aude Genevay, Gabriel Peyre, and Marco Cuturi. Learning generative models with sinkhorn divergences. In *Proceedings of the Twenty-First International Conference on Artificial Intelligence and Statistics*, pages 1608–1617. PMLR, 2018. [2](#), [5](#), [6](#)
- [17] Aude Genevay, Lénaïc Chizat, Francis Bach, Marco Cuturi, and Gabriel Peyré. Sample complexity of sinkhorn divergences, 2019. [2](#), [4](#)
- [18] Ian Goodfellow, Jean Pouget-Abadie, Mehdi Mirza, Bing Xu, David Warde-Farley, Sherjil Ozair, Aaron Courville, and Yoshua Bengio. Generative adversarial nets. In *Advances in Neural Information Processing Systems*. Curran Associates, Inc., 2014. [2](#)
- [19] Arthur Gretton, Karsten M. Borgwardt, Malte J. Rasch, Bernhard Schölkopf, and Alexander J. Smola. A kernel method for the two-sample problem. *CoRR*, abs/0805.2368, 2008. [5](#)
- [20] Ishaan Gulrajani, Faruk Ahmed, Martín Arjovsky, Vincent Dumoulin, and Aaron C. Courville. Improved training of wasserstein gans. *CoRR*, abs/1704.00028, 2017. [2](#), [4](#), [5](#)
- [21] He He and Wan-Chi Siu. Single image super-resolution using gaussian process regression. In *CVPR 2011*, pages 449–456, 2011. [2](#)
- [22] Kaiming He, Xiangyu Zhang, Shaoqing Ren, and Jian Sun. Deep residual learning for image recognition. *CoRR*, abs/1512.03385, 2015. [3](#)
- [23] Lingzhi He, Hongguang Zhu, Feng Li, Huihui Bai, Runmin Cong, Chunjie Zhang, Chunyu Lin, Meiqin Liu, and Yao Zhao. Towards fast and accurate real-world depth super-resolution: Benchmark dataset and baseline. *2021 IEEE/CVF Conference on Computer Vision and Pattern Recognition (CVPR)*, pages 9225–9234, 2021. [2](#), [7](#)
- [24] Antoine Houdard, Arthur Leclaire, Nicolas Papadakis, and Julien Rabin. On the existence of optimal transport gradient for learning generative models, 2021. [1](#)
- [25] Gao Huang, Zhuang Liu, and Kilian Q. Weinberger. Densely connected convolutional networks. *CoRR*, abs/1608.06993, 2016. [3](#)
- [26] Beomjun Kim, Jean Ponce, and Bumsuh Ham. Deformable kernel networks for joint image filtering. *International Journal of Computer Vision*, 129, 2021. [2](#), [7](#)
- [27] Dong-Eon Kim, Philippe Gourbesville, and Shie-Yui Liang. Overcoming data scarcity in flood hazard assessment using remote sensing and artificial neural network. *Smart Water*, 4:1–15, 2019. [1](#)
- [28] Christian Ledig, Lucas Theis, Ferenc Huszár, Jose Caballero, Andrew Cunningham, Alejandro Acosta, Andrew Aitken, Alykhan Tejani, Johannes Totz, Zehan

- Wang, and Wenzhe Shi. Photo-realistic single image super-resolution using a generative adversarial network. In *2017 IEEE Conference on Computer Vision and Pattern Recognition (CVPR)*, pages 105–114, 2017. 2
- [29] Jing Li and David Wong. Effect of dem sources on hydrologic applications. *Computers, Environment and Urban Systems*, 34:251–261, 2010. 1
- [30] Bee Lim, Sanghyun Son, Heewon Kim, Seungjun Nah, and Kyoung Mu Lee. Enhanced deep residual networks for single image super-resolution. *CoRR*, abs/1707.02921, 2017. 2
- [31] Huajun Liu, Fuqiang Liu, Xinyi Fan, and Dong Huang. Polarized self-attention: Towards high-quality pixel-wise regression. *CoRR*, abs/2107.00782, 2021. 4
- [32] Xiaoye Liu. Airborne lidar for dem generation: Some critical issues. *progress in physical geography. Progress in Physical Geography - PROG PHYS GEOG*, 32:31–49, 2008. 1
- [33] Nando Metzger, Rodrigo Caye Daudt, and Konrad Schindler. Guided depth super-resolution by deep anisotropic diffusion. *2023 IEEE/CVF Conference on Computer Vision and Pattern Recognition (CVPR)*, 2023. 2, 7
- [34] Gary Priestnall, Jad Jaafar, and A. Duncan. Extracting urban features from lidar digital surface models. *Computers, Environment and Urban Systems*, 24:65–78, 2000. 1
- [35] Matan Protter, Michael Elad, Hiroyuki Takeda, and Peyman Milanfar. Generalizing the nonlocal-means to super-resolution reconstruction. *IEEE Transactions on Image Processing*, 18(1):36–51, 2009. 2
- [36] Alec Radford, Luke Metz, and Soumith Chintala. Unsupervised representation learning with deep convolutional generative adversarial networks. *CoRR*, abs/1511.06434, 2015. 5
- [37] Litu Rout. Understanding the role of adversarial regularization in supervised learning. *CoRR*, abs/2010.00522, 2020. 5, 3, 4
- [38] Litu Rout, Indranil Misra, S Manthira Moorthi, and Debajyoti Dhar. S2a: Wasserstein gan with spatio-spectral laplacian attention for multi-spectral band synthesis, 2020. 4
- [39] Rasmus Sørensen and Jan Seibert. Effects of dem resolution on the calculation of topographical indices: Twi and its components. *Journal of Hydrology*, 347:79–89, 2007. 1
- [40] Hiroyuki Takeda, Sina Farsiu, and Peyman Milanfar. Kernel regression for image processing and reconstruction. *IEEE Transactions on Image Processing*, 16(2): 349–366, 2007. 2
- [41] Sebastiano Trevisani, Marco Cavalli, and Lorenzo Marchi. Surface texture analysis of a high-resolution dtm: Interpreting an alpine basin. *Geomorphology*, s 161–162:26–39, 2012. 1
- [42] U.S. Geological Survey (USGS). 1/3rd arc-second digital elevation models (dems)- usgs national map 3dep downloadable data collection. 2019. 6
- [43] Yifan Wang, Federico Perazzi, Brian McWilliams, Alexander Sorkine-Hornung, Olga Sorkine-Hornung, and Christopher Schroers. A fully progressive approach to single-image super-resolution. *CoRR*, abs/1804.02900, 2018. 3
- [44] Jonathan Weed and Francis Bach. Sharp asymptotic and finite-sample rates of convergence of empirical measures in wasserstein distance, 2017. 4
- [45] Zekai Xu, Xuewen Wang, Zixuan Chen, Xiong Dongping, Mingyue Ding, and Hou Wenguang. Nonlocal similarity based dem super resolution. *ISPRS Journal of Photogrammetry and Remote Sensing*, 110:48–54, 2015. 2
- [46] Zekai Xu, Zixuan Chen, Weiwei Yi, Qiuling Gui, Hou Wenguang, and Mingyue Ding. Deep gradient prior network for dem super-resolution: Transfer learning from image to dem. *ISPRS Journal of Photogrammetry and Remote Sensing*, 150:80–90, 2019. 2

SIRAN: Sinkhorn Distance Regularized Adversarial Network for DEM Super-Resolution using Discriminative Spatial Self-Attention

Supplementary Material

A. Proof of Theorem 1: Smoothness of Sinkhorn Loss

We will define some of the terminologies, which are necessary for this proof. From equation 6 of the main paper, the entropic optimal transport can be defined as, (\hat{y})

$$\begin{aligned} \mathcal{W}_{C,\varepsilon}(\mu_\theta, \nu) &= \inf_{\pi \in \Pi(\mu_\theta, \nu)} \int_{\mathcal{X} \times \mathcal{Y}} [C(\hat{y}, y)] d\pi(\hat{y}, y) \\ &\quad + \varepsilon I_\pi(\hat{y}, y), \\ \text{where } I_\pi(\hat{y}, y) &= \int_{\mathcal{X} \times \mathcal{Y}} \left[\log \left(\frac{\pi(\hat{y}, y)}{\mu_\theta(\hat{y}) \nu(y)} \right) \right] d\pi(\hat{y}, y), \\ \text{s.t. } \int_{\mathcal{X}} \pi(\hat{y}, y) dx &= \nu(y), \quad \int_{\mathcal{Y}} \pi(\hat{y}, y) dy = \mu_\theta(\hat{y}). \end{aligned} \quad (11)$$

where we assume $\hat{y} = \mathbf{G}_1 \theta(x)$ such that $\pi(\hat{y}, y) \geq 0$. The formulation in equation 11 corresponds to the primal problem of regularized OT and, this allows us to express the dual formulation of regularized OT as the maximization of an expectation problem, as shown in equation 12 [5].

$$\begin{aligned} \mathcal{W}_{C,\varepsilon}(\mu_\theta, \nu) &= \sup_{\phi, \psi \in \Phi} \int_{\mathcal{X}} \phi(\hat{y}) d\mu_\theta(\hat{y}) + \int_{\mathcal{Y}} \psi(y) d\nu(y) \\ &\quad - \varepsilon \int_{\mathcal{X} \times \mathcal{Y}} e^{\frac{\phi(\hat{y}) + \psi(y) - C(\hat{y}, y)}{\varepsilon}} d\mu_\theta(\hat{y}) d\nu(y) + \varepsilon, \end{aligned} \quad (12)$$

where $\Phi = \{(\phi, \psi) \in \mathcal{C}(\mathcal{X}) \times \mathcal{C}(\mathcal{Y})\}$ is set of real valued continuous functions for domain \mathcal{X} and \mathcal{Y} and they are referred as dual potentials. Now, given optimal dual potentials $\phi^*(\cdot)$, and $\psi^*(\cdot)$, the optimal coupling $\pi^*(\cdot)$ as per [5] can be defined as

$$\pi^*(\hat{y}, y) = \mu_\theta(\hat{y}) \nu(y) e^{\frac{\phi^*(\hat{y}) + \psi^*(y) - C(\hat{y}, y)}{\varepsilon}} \quad (13)$$

To prove **Theorem 2**, we need an important property regarding its Lipschitz continuity of the dual potentials, which is explained in the following **Lemma**.

Lemma A.1. *If $C(\cdot)$ is L_0 Lipschitz, then the dual potentials are also L_0 Lipschitz.*

Proof. As $\hat{y} = \mathbf{G}_\theta(x)$, $C(\hat{y}, y)$ is L_0 -Lipschitz in \hat{y} . As, the entropy $I_\pi(\cdot)$ is selected as Shannon entropy, according to [7] using the softmin operator, the optimal

potential $\phi^*(\cdot)$ satisfy the following equation

$$\phi^*(\hat{y}) = -\varepsilon \ln \left[\int_{\mathcal{Y}} \exp \left(\frac{\psi^*(y) - C(\hat{y}, y)}{\varepsilon} \right) dy \right] \quad (14)$$

Now, to estimate the Lipschitz of ϕ^* , we have to find the upper bound of $\|\nabla_{\hat{y}} \phi^*(\hat{y})\|$. Hence, taking the gradient of equation 4 with respect to p and its norm,

$$\|\nabla_{\hat{y}} \phi^*(\hat{y})\| = \frac{\left\| \int_{\mathcal{Y}} \exp \left(\frac{\psi^*(y) - C(\hat{y}, y)}{\varepsilon} \right) \nabla_{\hat{y}} C(\hat{y}, y) dy \right\|}{\left\| \int_{\mathcal{Y}} \exp \left(\frac{\psi^*(y) - C(\hat{y}, y)}{\varepsilon} \right) dy \right\|} \quad (15)$$

Now due to Lipschitz continuity of $C(\hat{y}, y)$, we can say $\|\nabla_{\hat{y}} C(\hat{y}, y)\| \leq L_0$. Hence, using Cauchy-Schwarz inequality we will get,

$$\begin{aligned} \|\nabla_{\hat{y}} \phi^*(\hat{y})\| &\leq \|\nabla_{\hat{y}} C(\hat{y}, y)\|. \\ \frac{\left\| \int_{\mathcal{Y}} \exp \left(\frac{\psi^*(y) - C(\hat{y}, y)}{\varepsilon} \right) dy \right\|}{\left\| \int_{\mathcal{Y}} \exp \left(\frac{\psi^*(y) - C(\hat{y}, y)}{\varepsilon} \right) dy \right\|} &= L_0. \end{aligned} \quad (16)$$

This completes the proof of the lemma. An alternative proof is provided in [24] in Proposition 4. Similarly, it can be proved for the other potential term. \square

For any $\theta_1, \theta_2 \in \Theta$ will result in different coupling solutions π_i^* , for $i = 1, 2$. Now, based on Danskins' theorem for optimal coupling $\pi^*(\theta)$, we can write

$$\nabla_\theta \mathcal{W}_{C,\varepsilon}(\mu_\theta, \nu) = \mathbb{E}_{\mathbf{G}_\theta(x), y \sim \pi^*(\theta)} [\nabla_\theta C(\mathbf{G}_\theta(x), y)] \quad (18)$$

Therefore, for any θ_1 and θ_2 , we can write,

$$\begin{aligned} &\|\nabla_\theta \mathcal{W}_{C,\varepsilon}(\mu_{\theta_1}, \nu) - \nabla_\theta \mathcal{W}_{C,\varepsilon}(\mu_{\theta_2}, \nu)\| \\ &\leq \|\mathbb{E}_{\mathbf{G}_{\theta_1}(x), y \sim \pi_1^*} [\nabla_\theta C(\mathbf{G}_{\theta_1}(x), y)] \\ &\quad - \mathbb{E}_{\mathbf{G}_{\theta_1}(x), y \sim \pi_2^*} [\nabla_\theta C(\mathbf{G}_{\theta_1}(x), y)]\| \\ &\quad + \|\mathbb{E}_{\mathbf{G}_{\theta_1}(x), y \sim \pi_2^*} [\nabla_\theta C(\mathbf{G}_{\theta_1}(x), y)] \\ &\quad - \mathbb{E}_{\mathbf{G}_{\theta_2}(x), y \sim \pi_2^*} [\nabla_\theta C(\mathbf{G}_{\theta_2}(x), y)]\| \\ &\leq L_0 L \|\pi_1^* - \pi_2^*\| + L_1 L \|\theta_1 - \theta_2\|. \end{aligned} \quad (19)$$

Now with respect to different θ_i , for $i = 1, 2$ with different pair of dual potentials, the $\|\pi_1^* - \pi_2^*\|$ can be written as below. For simplicity we denote $\mu_\theta \equiv \mu_\theta(\mathbf{G}_\theta(x))$, $\nu \equiv \nu(y)$, $\hat{y}_1 = \mathbf{G}_{\theta_1}(x)$, and $\hat{y}_2 = \mathbf{G}_{\theta_2}(x)$.

$$\begin{aligned}
& \|\pi_1^* - \pi_2^*\| \\
&= \|\mu_{\theta_1} \nu \exp\left(\frac{\phi^*(\hat{y}_1) + \psi^*(y) - C(\hat{y}_1, y)}{\varepsilon}\right) \\
&\quad - \mu_{\theta_2} \nu \exp\left(\frac{\phi^*(\hat{y}_2) + \psi^*(y) - C(\hat{y}_2, y)}{\varepsilon}\right)\| \\
&\leq \|\nu \exp\left(\frac{\phi^*(\hat{y}_1) + \psi^*(y) - C(\hat{y}_1, y)}{\varepsilon}\right) (\mu_{\theta_1} - \mu_{\theta_2})\| \\
&\quad + \|\mu_{\theta_2} \nu \left[\exp\left(\frac{\phi^*(\hat{y}_1) + \psi^*(y) - C(\hat{y}_1, y)}{\varepsilon}\right) \right. \\
&\quad \left. - \exp\left(\frac{\phi^*(\hat{y}_2) + \psi^*(y) - C(\hat{y}_2, y)}{\varepsilon}\right) \right]\|. \quad (20)
\end{aligned}$$

From [17], we know, as the dual potentials are L_0 -Lipschitz, $\forall \mathbf{G}_\theta(x) \in \mathcal{X}$, we can write, $\phi^*(\mathbf{G}_\theta(x)) \leq L_0|\mathbf{G}_\theta(x)|$. And from property of c-transform, for $\forall y \in \mathcal{Y}$ we can also write $\psi^*(y) \leq \max_{\mathbf{G}_\theta(x)} \phi^*(\mathbf{G}_\theta(x)) - C(\mathbf{G}_\theta(x), y)$. We assume \mathcal{X} to be a bounded set in our case, hence, denoting $|\mathcal{X}|$ as the diameter of the space, at optimality, we can get that $\forall \mathbf{G}_\theta(x) \in \mathcal{X}$, $y \in \mathcal{Y}$

$$\begin{aligned}
&\Rightarrow \phi^*(\mathbf{G}_\theta(x)) + \psi^*(y) \leq 2L_0|\mathcal{X}| + \|C\|_\infty \\
&\Rightarrow \exp\left(\frac{\phi^*(\mathbf{G}_\theta(x)) + \psi^*(y) - C(\mathbf{G}_\theta(x), y)}{\varepsilon}\right) \\
&\leq \exp\left(2\frac{L_0|\mathcal{X}| + \|C\|_\infty}{\varepsilon}\right). \quad (21)
\end{aligned}$$

Hence, the exponential terms in equation 20 are bounded, and we can assume it has a finite Lipschitz constant L_{exp} . Taking $\kappa = 2(L_0|\mathcal{X}| + \|C\|_\infty)$, and using Cauchy-Schwarz, we can rewrite equation 20 as,

$$\begin{aligned}
\|\pi_1^* - \pi_2^*\| &\leq \exp\left(\frac{\kappa}{\varepsilon}\right) \|\nu\| \cdot \|\mu_{\theta_1} - \mu_{\theta_2}\| \\
&\quad + \frac{L_{exp} \|\mu_{\theta_2}\| \cdot \|\nu\|}{\varepsilon} \|(\phi^*(\hat{y}_1) - \phi^*(\hat{y}_2)) \\
&\quad - (C(\hat{y}_1, y) - C(\hat{y}_2, y))\| \\
&\leq \exp\left(\frac{\kappa}{\varepsilon}\right) \|\nu\| \cdot \|\mu_{\theta_1} - \mu_{\theta_2}\| \\
&\quad + 2\frac{L_{exp} L_0 L}{\varepsilon} \|\mu_{\theta_2}\| \cdot \|\nu\| \cdot \|\theta_1 - \theta_2\|. \quad (22)
\end{aligned}$$

Now, as the input space \mathcal{X} and output space \mathcal{Y} are bounded, the corresponding measures μ_θ and ν will also be bounded. We assume, $\|\mu_\theta\| \leq \lambda_1$ and $\|\nu\| \leq \lambda_2$. If we apply equation 21 in equation 13, to get the upper bound of the coupling function, we will get $\|\pi_1^* - \pi_2^*\| \leq \exp\left(\frac{\kappa}{\varepsilon}\right) \|\nu\| \cdot \|\mu_{\theta_1} - \mu_{\theta_2}\|$ which is less than the bound in equation 22. Then, we can find some constant upper bound of $\|\pi_1^* - \pi_2^*\|$, using the assumed bounds of measures and can write $\|\pi_1^* - \pi_2^*\| \leq \exp\left(\frac{\kappa}{\varepsilon}\right) \|\nu\| \cdot \|\mu_{\theta_1} -$

$\mu_{\theta_2}\| \leq K$, such that,

$$\begin{aligned}
K &\leq \exp\left(\frac{\kappa}{\varepsilon}\right) \|\nu\| \cdot \|\mu_{\theta_1} - \mu_{\theta_2}\| \\
&\quad + 2\frac{L_{exp} L_0 L}{\varepsilon} \|\mu_{\theta_2}\| \cdot \|\nu\| \cdot \|\theta_1 - \theta_2\|. \quad (23)
\end{aligned}$$

Then using the marginal condition as shown in equation 11, we can write equation 22 as,

$$\begin{aligned}
K &\leq \lambda_1 \exp\left(\frac{\kappa}{\varepsilon}\right) \left\| \int_{\mathcal{X}} \pi_1^* dx - \int_{\mathcal{X}} \pi_2^* dx \right\| \\
&\quad + 2\lambda_1 \lambda_2 \frac{L_{exp} L_0 L}{\varepsilon} \|\theta_1 - \theta_2\| \\
&\leq \lambda_1 \exp\left(\frac{\kappa}{\varepsilon}\right) \int_{\mathcal{X}} \|\pi_1^* - \pi_2^*\| \cdot |dx| \\
&\quad + 2\lambda_1 \lambda_2 \frac{L_{exp} L_0 L}{\varepsilon} \|\theta_1 - \theta_2\| \\
&\leq \lambda_1 \exp\left(\frac{\kappa}{\varepsilon}\right) K \int_{\mathcal{X}} |dx| \\
&\quad + 2\lambda_1 \lambda_2 \frac{L_{exp} L_0 L}{\varepsilon} \|\theta_1 - \theta_2\|. \quad (24)
\end{aligned}$$

The input set is a compact set such that $\mathcal{X} \subset \mathbb{R}^d$. So, assuming m and M to be the minimum and maximum value in set \mathcal{X} and considering the whole situation in discrete space, equation 24 can be rewritten as,

$$\begin{aligned}
K &\leq \lambda_1 \exp\left(\frac{\kappa}{\varepsilon}\right) K \sum_{x \in \mathcal{X}} |x| + 2\lambda_1 \lambda_2 \frac{L_{exp} L_0 L}{\varepsilon} \|\theta_1 - \theta_2\| \\
&\leq \lambda_1 \exp\left(\frac{\kappa}{\varepsilon}\right) K d \max(|M|, |m|) \\
&\quad + 2\lambda_1 \lambda_2 \frac{L_{exp} L_0 L}{\varepsilon} \|\theta_1 - \theta_2\|. \quad (25)
\end{aligned}$$

Now, taking $B = d \max(|M|, |m|)$, and doing necessary subtraction and division on both sides of equation 25, it can be rewritten as

$$\begin{aligned}
K &\leq \frac{2\lambda_1 \lambda_2 L_{exp} L_0 L}{\varepsilon (1 - \lambda_1 B \exp\left(\frac{\kappa}{\varepsilon}\right))} \|\theta_1 - \theta_2\| \\
&\leq \frac{2\lambda_1 \lambda_2 L_{exp} L_0 L}{\varepsilon (1 + \lambda_1 B \exp\left(\frac{\kappa}{\varepsilon}\right))} \|\theta_1 - \theta_2\| \quad (26)
\end{aligned}$$

Equation 26 satisfies because $\frac{\kappa}{\varepsilon} \geq 0$. As, $\|\pi_1^* - \pi_2^*\| \leq K$, from equation 26, it can be written as

$$\|\pi_1^* - \pi_2^*\| \leq \frac{2\lambda_1 \lambda_2 L_{exp} L_0 L}{\varepsilon (1 + \lambda_1 B \exp\left(\frac{\kappa}{\varepsilon}\right))} \|\theta_1 - \theta_2\| \quad (27)$$

Substituting equation 27 in equation 19, we will get,

$$\begin{aligned}
&\|\nabla_\theta \mathcal{W}_{C, \varepsilon}(\mu_{\theta_1}, \nu) - \nabla_\theta \mathcal{W}_{C, \varepsilon}(\mu_{\theta_2}, \nu)\| \\
&\leq L_0 L \|\pi_1^* - \pi_2^*\| + L_1 L \|\theta_1 - \theta_2\| \\
&\leq \left(L_1 L + \frac{2\lambda_1 \lambda_2 L_{exp} L_0^2 L^2}{\varepsilon (1 + \lambda_1 B \exp\left(\frac{\kappa}{\varepsilon}\right))} \right) \|\theta_1 - \theta_2\| \quad (28)
\end{aligned}$$

So, the EOT problem defined in equation 11 has $\hat{\Gamma}_\varepsilon$ smoothness in θ with $\hat{\Gamma}_\varepsilon = L_1 L + \frac{2\lambda_1 \lambda_2 L_{\text{exp}} L_0^2 L^2}{\varepsilon(1 + \lambda_1 B \exp(\frac{\kappa}{\varepsilon}))}$. From this, we can derive the smoothness of Sinkhorn loss defined in equation 7 of the main paper. Note that only the first two terms in equation 7 of the main paper are θ dependent. Therefore, they only contribute to the gradient approximation and both of them will satisfy the same smoothness condition as defined in equation 28. So, if sinkhorn loss has smoothness Γ_ε , it will satisfy, $\Gamma_\varepsilon = \frac{3}{2} \hat{\Gamma}_\varepsilon$. In general, we can define the smoothness of sinkhorn loss with $(\theta_1, \theta_2) \in \Theta$ as,

$$\begin{aligned} & \|\nabla_\theta S_{C,\varepsilon}(\mu_{\theta_1}, \nu) - \nabla_\theta S_{C,\varepsilon}(\mu_{\theta_2}, \nu)\| \\ & \leq \mathcal{O}\left(L_1 L + \frac{2L_0^2 L^2}{\varepsilon(1 + B \exp(\frac{\kappa}{\varepsilon}))}\right) \|\theta_1 - \theta_2\| \end{aligned} \quad (29)$$

This completes proof of the statement in **Theorem 2**

B. Proof of Proposition 1

This proof is inspired by [37]. Assuming $\Gamma = \mathcal{O}\left(L_1 + \frac{2L_0^2}{\varepsilon(1 + B \exp(\frac{\kappa}{\varepsilon}))}\right)$ be the smoothness in p for Sinkhorn loss $S_{C,\varepsilon}(\mu_\theta(p), \nu(y))$, where $p = \mathbf{G}_\theta(x)$. For simplicity, we use a common set for inputs and outputs as \mathcal{P} . Hence, to approximate the gradient of sinkhorn loss, using Jensen's inequality, we can write,

$$\begin{aligned} & \|\nabla_\theta \mathbb{E}_{(x,y) \sim \mathcal{P}} [S_{C,\varepsilon}(\mu_\theta(\mathbf{G}_\theta(x)), \nu(y))]\| \\ & \leq \mathbb{E}_{(x,y) \sim \mathcal{P}} [\|\nabla_\theta S_{C,\varepsilon}(\mu_\theta(\mathbf{G}_\theta(x)), \nu(y))\|] \\ & \leq \mathbb{E}_{(x,y) \sim \mathcal{P}} \left[\underbrace{\|\nabla_p S_{C,\varepsilon}(\mu_\theta(p), \nu(y))\| \cdot \|\nabla_\theta \mathbf{G}_\theta(x)\|}_{\text{Cauchy-Schwarz inequality}} \right] \\ & \leq L \mathbb{E}_{(x,y) \sim \mathcal{P}} [\|\nabla_p S_{C,\varepsilon}(\mu_\theta(p), \nu(y))\|] \end{aligned} \quad (30)$$

Say, for optimized parameter θ^* , $t = \mathbf{G}_{\theta^*}(x)$. Since, $\|\theta - \theta^*\|$, we can write using the smoothness of sinkhorn loss and Lipschitz of model parameters,

$$\begin{aligned} & \|\nabla_p S_{C,\varepsilon}(\mu_\theta(p), \nu(y))\| - \|\nabla_t S_{C,\varepsilon}(\mu_{\theta^*}(t), \nu(y))\| \\ & \leq \|\nabla_p S_{C,\varepsilon}(\mu_\theta(p), \nu(y)) - \nabla_t S_{C,\varepsilon}(\mu_{\theta^*}(t), \nu(y))\| \\ & \leq \Gamma \|p - t\| = \Gamma \|\mathbf{G}_\theta(x) - \mathbf{G}_{\theta^*}(x)\| \\ & \leq \Gamma L \|\theta - \theta^*\| \leq \Gamma L \varepsilon \end{aligned} \quad (31)$$

At optimal condition, $\|\nabla_t S_{C,\varepsilon}(\mu_{\theta^*}(t), \nu(y))\| = 0$ as the distributions of y and $t = \mathbf{G}_{\theta^*}(x)$ are aligned for optimal θ^* . So, by substituting equation 31 in equation 30, we will get

$$\|\nabla_\theta \mathbb{E}_{(x,y) \sim \mathcal{P}} [S_{C,\varepsilon}(\mu_\theta(\mathbf{G}_\theta(x)), \nu(y))]\| \leq L^2 \Gamma \varepsilon \quad (32)$$

From Lemma 1 of [37], we get,

$$\|\nabla_\theta \mathbb{E}_{(x,y) \sim \mathcal{P}} [l(\mathbf{G}_\theta(x), y)]\| \leq L^2 \beta \varepsilon \quad (33)$$

Similarly, from Lemma 2 of [37], we get

$$\|-\nabla_\theta \mathbb{E}_{(x,y) \sim \mathcal{P}} [g(\psi; \mathbf{G}_\theta(x))]\| \leq L \delta \quad (34)$$

Here, ψ is parameters of discriminator \mathbf{D} . So using equations 32, 33, and 34, for the combination of losses we will get,

$$\begin{aligned} & \|\nabla_\theta \mathbb{E}_{(x,y) \sim \mathcal{P}} [l(\mathbf{G}_\theta(x), y) + S_{C,\varepsilon}(\mu_\theta(\mathbf{G}_\theta(x)), \nu(y)) \\ & - g(\psi; \mathbf{G}_\theta(x))]\| \leq \|\nabla_\theta \mathbb{E}_{(x,y) \sim \mathcal{P}} [l(\mathbf{G}_\theta(x), y)]\| \\ & + \|\nabla_\theta \mathbb{E}_{(x,y) \sim \mathcal{P}} [S_{C,\varepsilon}(\mu_\theta(\mathbf{G}_\theta(x)), \nu(y))]\| \\ & + \|\nabla_\theta \mathbb{E}_{(x,y) \sim \mathcal{P}} [g(\psi; \mathbf{G}_\theta(x))]\| \\ & \leq L^2 \beta \varepsilon + L^2 \Gamma \varepsilon + L \delta = L^2 \varepsilon (\beta + \Gamma) + L \delta \end{aligned} \quad (35)$$

This completes the proof of **Proposition 1**.

C. Proof of Proposition 2

This proof also follows the steps of Theorem 3 from [37]. In the sinkhorn regularized adversarial setup, the parameters θ are updated using fixed step gradient descent. They iterate as,

$$\theta_{t+1} = \theta_t - h_t \nabla(l(\theta_t) + S_{C,\varepsilon}(\mu_{\theta_t}(\mathbf{G}_{\theta_t}(x)), \nu(y)) - g(\psi; \mathbf{G}_{\theta_t}(x))). \quad (36)$$

For simplicity, we denote $S_{C,\varepsilon}(\mu_{\theta_t}(\mathbf{G}_{\theta_t}(x)), \nu(y)) \equiv S_{C,\varepsilon}(\mu_{\theta_t}, \nu)$. Using Taylor's expansion,

$$\begin{aligned} l(\theta_{t+1}) & = l(\theta_t) + \nabla l(\theta_t)(\theta_{t+1} - \theta_t) \\ & + \frac{1}{2}(\theta_{t+1} - \theta_t)^T \nabla^2 l(\theta_t)(\theta_{t+1} - \theta_t). \end{aligned} \quad (37)$$

Now, substituting $\theta_{t+1} - \theta_t$ from equation 36, and using triangle inequality and Cauchy-Schwarz inequality, equation 37 can be rewritten as,

$$\begin{aligned} l(\theta_{t+1}) & \leq \\ & l(\theta_t) - h_t \|\nabla l(\theta_t)\|^2 - h_t \|\nabla l(\theta_t)\| \cdot \|\nabla S_{C,\varepsilon}(\mu_{\theta_t}, \nu)\| \\ & - h_t \|\nabla l(\theta_t)\| \cdot \|g(\psi; \mathbf{G}_{\theta_t}(x))\| + h_t^2 \|\nabla l(\theta_t)\| \\ & + S_{C,\varepsilon}(\mu_{\theta_t}, \nu) - g(\psi; \mathbf{G}_{\theta_t}(x))\|^2 \frac{\|\nabla^2 l(\theta_t)\|}{2}. \end{aligned} \quad (38)$$

Taking into account the assumptions in **Proposition 2** and utilizing Minkowski's inequality, equation 38 can be rewritten as,

$$\begin{aligned} l(\theta_{t+1}) & \leq \\ & l(\theta_t) - h_t \|\nabla l(\theta_t)\|^2 - h_t \|\nabla l(\theta_t)\| \eta \\ & - h_t \|\nabla l(\theta_t)\| \zeta + h_t^2 (\|\nabla l(\theta_t)\|^2 + \|S_{C,\varepsilon}(\mu_{\theta_t}, \nu)\|^2 \\ & + \|g(\psi; \mathbf{G}_{\theta_t}(x))\|^2) \frac{\beta_1}{2}. \end{aligned} \quad (39)$$

Using $h_t = \frac{1}{\beta_1}$, from equation 39, we can write,

$$\begin{aligned}
l(\theta_{t+1}) &\leq l(\theta_t) - \frac{h_t \|\nabla l(\theta_t)\|^2}{2} - h_t \|\nabla l(\theta_t)\| \eta \\
&\quad - h_t \|\nabla l(\theta_t)\| \zeta + \frac{h_t \|S_{C,\varepsilon}(\mu_{\theta_t}, \nu)\|^2}{2} \\
&\quad + \frac{h_t \|g(\psi; \mathbf{G}_{\theta_t}(x))\|^2}{2} \\
&\leq l(\theta_t) - \frac{h_t \epsilon_1^2}{2} - h_t \epsilon_1 \eta - h_t \epsilon_1 \zeta \\
&\quad + \frac{h_t L^4 \Gamma^2 \epsilon^2}{2} + \frac{h_t L^2 \delta^2}{2}. \tag{40}
\end{aligned}$$

Assuming T iterations to reach this ϵ_1 -stationary point, then for $t \leq T$, doing telescopic sum over t ,

$$\begin{aligned}
&\sum_{t=0}^{T-1} l(\theta_{t+1}) - l(\theta_t) \\
&\leq \frac{-T(\epsilon_1^2 + 2\epsilon_1(\zeta + \eta) - L^2(\delta^2 + L^2\Gamma^2\epsilon^2))}{2\beta_1} \\
&\Rightarrow T \leq \frac{2(l(\theta_0) - l^*)\beta_1}{(\epsilon_1^2 + 2\epsilon_1(\zeta + \eta) - L^2(\delta^2 + L^2\Gamma^2\epsilon^2))}. \tag{41}
\end{aligned}$$

Therefore, using the iteration complexity definition of [37], we obtain,

$$\begin{aligned}
&\sup_{\theta_0 \in \{\mathbb{R}^{h \times d_x}, \mathbb{R}^{d_y \times h}\}, l \in \mathcal{L}} \mathcal{T}_{\epsilon_1}(A_h[l, \theta_0], l) \\
&= \mathcal{O}\left(\frac{(l(\theta_0) - l^*)\beta_1}{\epsilon_1^2 + 2\epsilon_1(\zeta + \eta) - L^2(\delta^2 + L^2\Gamma^2\epsilon^2)}\right). \tag{42}
\end{aligned}$$

This completes the proof of **Proposition 2**.

C.1. Proof of Corollary 1

Using the similar arguments of **Proposition 2**, and taking first-order Taylor's approximation, we get

$$\begin{aligned}
l(\theta_{t+1}) &= l(\theta_t) - h_t \|\nabla l(\theta_t)\|^2 - h_t \|\nabla l(\theta_t)\| \\
&\quad \cdot \|\nabla S_{C,\varepsilon}(\mu_{\theta_t}, \nu)\| - h_t \|\nabla l(\theta_t)\| \cdot \|g(\psi; \mathbf{G}_{\theta_t}(x))\| \\
&\leq l(\theta_t) - h_t \epsilon_1^2 - h_t \epsilon_1 \eta - h_t \epsilon_1 \zeta \tag{43}
\end{aligned}$$

Taking telescopic sum over t for $t \leq T$, we get

$$\sum_{t=0}^{T-1} l(\theta_{t+1}) - l(\theta_t) \leq -Th_t(\epsilon_1^2 + \epsilon_1(\zeta + \eta)) \tag{44}$$

So, using the definition of iteration complexity, we get,

$$\begin{aligned}
&\sup_{\theta_0 \in \{\mathbb{R}^{h \times d_x}, \mathbb{R}^{d_y \times h}\}, l \in \mathcal{L}} \mathcal{T}_{\epsilon_1}(A_h[l, \theta_0], l) \\
&= \mathcal{O}\left(\frac{l(\theta_0) - l^*}{\epsilon_1^2 + \epsilon_1(\zeta + \eta)}\right) \tag{45}
\end{aligned}$$

This completes the proof of **Corollary 2**.

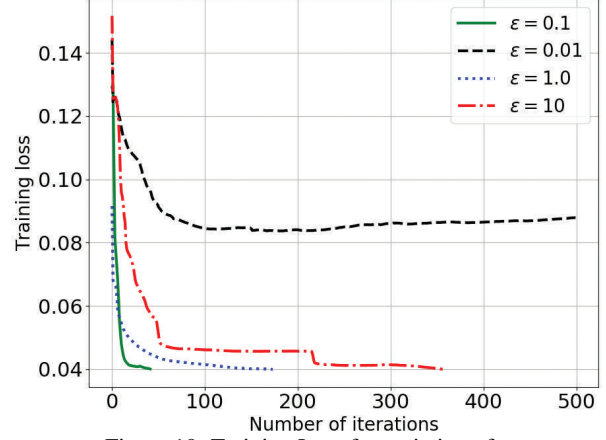


Figure 10. Training Loss for variation of ε

D. Experiments

We perform experiments to answer the proposed claims in our paper. There are two main aspects we want to investigate, firstly, how the choice of ε affects the overall training of the model, and secondly, how it performs compared to other state-of-the-art learning methods like WGAN, WGAN+GP, and DCGAN. In both these cases, we analyze the claims of mitigating vanishing gradients in the near-optimal region and fast convergence rate.

D.1. Implementation details

In this setting, we are performing a denoising operation on the MNIST dataset. For this 60000 samples of size 28×28 are used during training, while 10000 are used for testing. The convergence criterion is set to be the mean square error of 0.04 or a maximum of 500 epochs. During training, we randomly add Gaussian noise to the training samples to perform the denoising task. The generator is designed as a simple autoencoder structure with an encoder and decoder each having 2 convolutional layers. In practice, we notice that a discriminator with shallow layers is usually sufficient to offer a higher convergence rate. Therefore, we choose, a three-layer fully connected network with 1024 and 256 hidden neurons. All the layers are followed by ReLU activation except the output layer. For optimization, ADAM is utilized with a learning rate of 0.001 with a batch size of 64, and the discriminator is updated once for every single update of the generator.

D.2. Results analysis

Figure 10, shows how changing the value of ε affects the overall iteration complexity. According to this figure, the instances ε are very small and very large, and the learning behavior of the model becomes close to regular

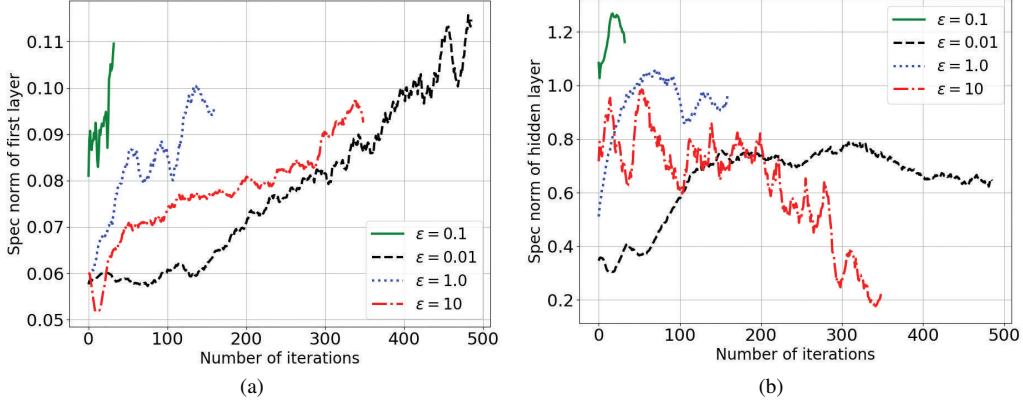


Figure 11. Approximated Spectral norm of gradients of (a) first layer, (b) hidden layer for different values of ε

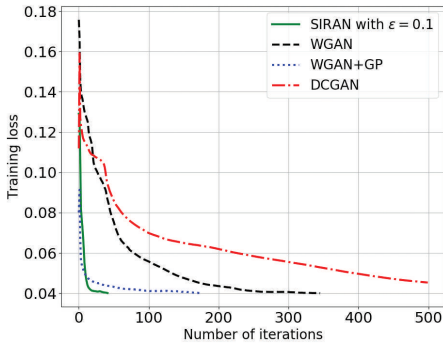


Figure 12. Training Loss for different learning methods

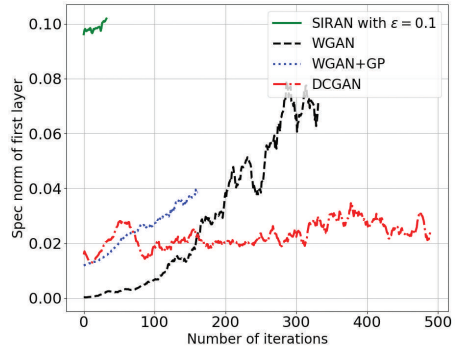


Figure 13. Approx. Spec norm of gradients of first layer

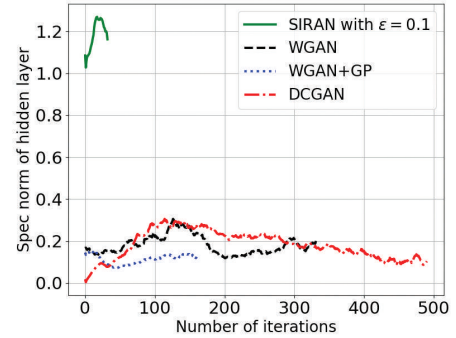


Figure 14. Approx Spec norm of gradients of hidden layer

adversarial setup which ultimately results in more time requirement for convergence. This is because, as $\varepsilon \rightarrow 0$ and $\varepsilon \rightarrow \infty$, the smoothness of sinkhorn loss tends to become independent of ε as depicted in **Theorem 1**, which makes the overall setup similar to the regular adversarial framework. This also affects the capability of mitigating the vanishing gradient problem as shown in Figure 2. The gradients are approximated using spectral norm and they are moving averaged for better visualization. From Figure 11(a), in the case of the first layer, as ε varies, the estimated gradients are similar near the optimal region. However, From Figure 11(b), we can see for the case of the hidden layer, gradient approximation is definitely affected by the choice of ε , and we can see as $\varepsilon \rightarrow 0$ and $\varepsilon \rightarrow \infty$, the gradients near-optimal region become smaller. However, using $\varepsilon = 0.1$ tends to have higher gradients even if near the optimal region. Therefore, this model will have more capability of mitigating the vanishing gradient problem. Hence, we use this model to compare with other benchmark methods.

We compare the rate of convergence and capability of handling the vanishing gradient of SIRAN with WGAN [3], WGAN+GP [20], and DCGAN [36]. Figure 3 clearly visualizes how our proposed framework

has tighter iteration complexity than others, and reaches the convergence faster. This is consistent with the theoretical analysis presented in **Proposition 3**. Figure 4, also provides empirical evidence of the vanishing gradient issue presented in **Proposition 2**. Both for the first layer and hidden layer, as shown in Figure 4, the approximated gradients are higher comparatively than others near the optimal region. This results in increasing the effectiveness of SIRAN in handling the issue of the vanishing gradient problem as discussed in Section 3.2.2 in the main paper.